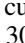

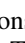




The Mysterious Location of Maryland on 2014 MU69 and the Reconfiguration of Its Bilobate Shape

Masatoshi Hirabayashi¹ , Alexander J. Trowbridge² , and Dennis Bodewits³ 

¹ Auburn University, 211 Davis Hall, Auburn, AL 36849, USA; thirabayashi@auburn.edu

² Purdue University, 550 Stadium Mall Drive, West Lafayette, IN 47907, USA

³ Auburn University, Physics Department, Leach Science Center, Auburn, AL 36832, USA

Received 2019 July 16; revised 2019 August 26; accepted 2019 August 27; published 2020 February 28

Abstract

2014 MU69 (named Arrokoth), targeted by *New Horizons*, has a unique bilobate shape. Research suggested that there is a large circular depression feature with a diameter of ~ 7 km on the smaller lobe of this object. This feature, called Maryland, is surrounded by topographically high regions and faces perpendicular to the shortest axis of this object. Here, following the interpretation by earlier work that Maryland is formed by an impact, we investigate how the Maryland impact affects the structure of a neck of this object. We find that to avoid a structural breakup driven by this impact, MU69 needs high cohesive strength, at least tens of kilopascals depending on the bulk density. The cohesive strength at this level is much higher than that of other small bodies observed at high resolution, which is usually reported to be a few hundred pascals. It may be possible that MU69 actually has such a high cohesive strength, which may challenge the current knowledge about the cohesive strength of small bodies. Alternatively, we hypothesize a scenario that the Maryland impact actually broke the neck structure and made the shape settle into the current configuration. Considering this scenario, we obtain that the bulk density of MU69 should be between 300 and 500 kg m⁻³.

Unified Astronomy Thesaurus concepts: Asteroids (72); Comets (280); Comet interiors (272); Kuiper belt (893); Centaurs (215)

1. Introduction

Many trans-Neptunian objects (TNOs) are reported to be equal-sized bilobate objects (Thirouin & Sheppard 2019a, 2019b). Bilobate TNOs may form due to multiple different processes (e.g., Davidsson et al. 2016; Morbidelli & Nesvorný 2019). One scenario is soft merging of primordial lobes (e.g., Davidsson et al. 2016). In this scenario, gas and dust particles in the solar nebula accumulate by collisional agglomeration (e.g., Birnstiel et al. 2016) or by gravitational instability (e.g., Johansen et al. 2007; Nesvorný et al. 2010), leading to the formation of primordial binary systems (e.g., Fraser et al. 2017). Another scenario is that catastrophic collisions directly produce binary systems, followed by the formation of bilobate shapes (e.g., Jutzi & Benz 2017; Schwartz et al. 2018). Either way, two components may eventually merge softly when their mutual orbit is dynamically unstable (e.g., Scheeres 2007).

Bilobate objects are more structurally vulnerable than round objects because of their necks (Hirabayashi & Scheeres 2019). The spin states of cometary nuclei can rapidly evolve due to outgassing activities (Bodewits et al. 2018). Depending on their structural conditions, bilobate objects may end up in fission (Scheeres 2007). The fate of the split components depends on the energy of the system (Jacobson & Scheeres 2011). If the energy is positive, these elements may eventually escape from each other (Jacobson & Scheeres 2011). This dynamics analysis was applied to explain a shape reconfiguration process of the bilobate nucleus of comet 67P/Churyumov–Gerasimenko (Hirabayashi et al. 2016).

The close flyby of 2014 MU69 (also known as Arrokoth), a cold class Kuiper Belt Object (KBO), by the *New Horizons* spacecraft in 2019 showed that this object has a unique bilobate shape that consists of smoothed surfaces, hexagonal patches, and multiple crater-like features (e.g., Schenk et al. 2019; Singer et al. 2019;

Stern et al. 2019). MU69’s structure is likely to be icy and highly porous (Stern et al. 2019). Among the crater-like features, Maryland, a circular depression enclosed by topographically high regions, is likely to be a crater with a diameter of ~ 7 km (Singer et al. 2019; Stern et al. 2019). In this study, assuming that Maryland formed after the formation of MU69’s bilobate shape, we explore how much cohesive strength was necessary for the neck to resist structural disturbance by the Maryland impact event.

2. Model Formulation

We combine an impact crater scaling model (Model I) and a dynamics and structure model (Model II). We assume MU69’s shape to consist of a triaxial ellipsoid and a sphere. The larger lobe of MU69 is a triaxial ellipsoid with a size of $22 \times 20 \times 7$ km, while the smaller lobe is a sphere with an equivalent radius, R_S , of 6.3 km (Stern et al. 2019). The bulk density is a free parameter in the following discussion.

2.1. Impact Crater Scaling Model (Model I)

Applying the π -scaling relationship by Holsapple (1993), Model I computes the linear momentum that generates the Maryland crater on the smaller lobe. Unfortunately, the material properties of MU69 are not well known, and thus proper scaling parameters are not available. To give constraints on the impact behavior in the gravity and strength regimes on this body, we consider two endmember target material groups. Endmember A consists of a porous sand target (Wünnemann et al. 2006) and an icy, porous target (Arakawa & Yasui 2011) in the strength regime. Endmember B includes a water-ice target (Kraus et al. 2011) in the gravity regime and an icy, porous target (Arakawa & Yasui 2011) in the strength regime.

In the gravity regime, the scaling relationship is provided as (Wünnemann et al. 2006; Kraus et al. 2011)

$$\pi_V = C_g \pi_2^{-\beta_g}, \quad (1)$$

where C_g and β_g are empirical parameters. π_V characterizes the volume of the transient crater cavity, while $\pi_2 = g/v_i^2 \times (4\pi r_i^3/3)^{1/3}$, where g is the surface gravity, v_i is the impact speed, and r_i is the impactor radius (Holsapple 1993). Note that because Wünnemann et al. (2006) and Kraus et al. (2011) used π_D , where $\pi_D = (24\pi_V/\pi)^{1/3}$ (Richardson et al. 2007), instead of π_V , we properly convert their empirical parameters in our study. In the strength regime, on the other hand, the scaling relationship is written as (Arakawa & Yasui 2011)

$$\pi_V = C_Y \pi_3^{*- \beta_Y}, \quad (2)$$

where C_Y and β_Y are empirically determined. π_3^* is given as

$$\pi_3^* = \frac{K_2 Y}{p_0}, \quad (3)$$

where Y is the material strength, and p_0 is defined as

$$p_0 = \frac{\rho_t C_{0t} v_i}{1 + \frac{\rho_t C_{0t}}{\rho_i C_{0i}}}. \quad (4)$$

C_{0t} and C_{0i} are the sound speeds in the target and the impactor, respectively. We use the sound speed in bubble-free water ice for C_{0t} and that in olivine-rich dunite for C_{0i} . For the bubble-free water-ice structure, the sound speed is 1.85 km s^{-1} at a temperature of 260 K, and it may be higher with the decrease of temperature (Vogt et al. 2008). For the dunite structure, the sound speed is 4.5 km (Christensen 1966). Also, ρ_t and ρ_i are the bulk densities of the target and the impactor, respectively. In this study, ρ_i is fixed at 2000 kg m^{-3} .

We apply the π_V parameter by Holsapple (1993) to smoothly connect the scaling relationship in the gravity regime (Wünnemann et al. 2006; Kraus et al. 2011) and that in the strength regime (Arakawa & Yasui 2011). The classical form of the π_V parameter by Holsapple (1993), however, violates the smooth connection between the two regimes because there are fewer parameters in his expression than necessary. To avoid this issue, we update his π_V parameter and write it as

$$\pi_V = K_1 [\pi_2 \pi_4^{-\frac{1}{3}} + (K_2 \pi_3^*)^\gamma]^{-\frac{3\mu}{2+\mu}}, \quad (5)$$

where K_1 , K_2 , and μ are empirical parameters, and $\pi_4 = \rho_t/\rho_i$. γ is a new parameter that allows for incorporating the scaling relationship for an icy, porous target by Arakawa & Yasui (2011) in the strength regime. Note that in the classical form of π_V , π_3^* and γ are identical to $\pi_3 = Y/(\rho_t v_i^2)$ and $(2+\mu)/2$, respectively (Holsapple 1993; Richardson et al. 2007). We determine K_1 , K_2 , μ , and γ so that Equations (1), (2) asymptotically correspond to Equation (5) in each regime.

Using Equation (5), we obtain the transient crater diameter, D_{tr} , as (Richardson et al. 2007)

$$D_{tr} = \left(\frac{24 m_i}{\pi \rho_t} \pi_V \right)^{\frac{1}{3}}, \quad (6)$$

where m_i is the mass of the impactor. We next compute the final crater diameter, D_f . A typical value of D_f/D_{tr} for terrestrial

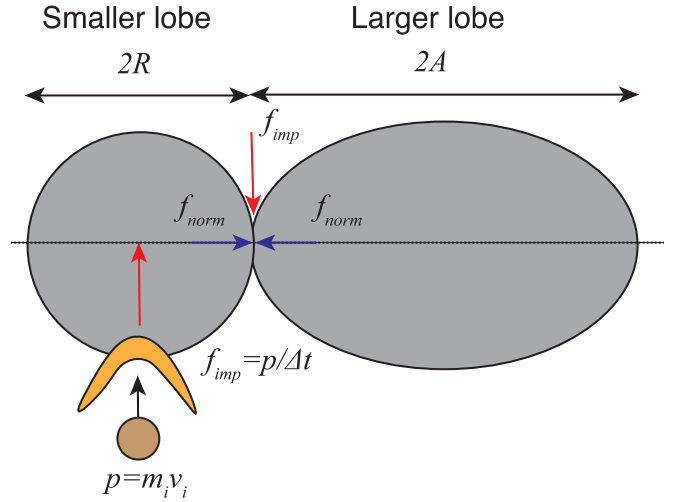


Figure 1. Schematic of the force balance during the Maryland impact. The dashed line defines the direction along the long axis of the modeled MU69.

craters may be ~ 1.1 – 1.3 (Melosh 1989), although this can strongly be dependent on the gravitational collapse of crater walls (Kraus et al. 2011). Here, we use the scaling relationship for an icy target by Kraus et al. (2011), who gave

$$D_f = (1.3\kappa)^{\frac{1}{1-\eta}} \left(\frac{D_{tr}}{D_{sc}} \right)^{\frac{\eta}{1-\eta}} D_{tr}, \quad (7)$$

where $\kappa = 1.19$ and $\eta = 0.04$. D_{sc} is the transition diameter from a simple crater to a complex crater. To determine D_{sc} for MU69, we follow the technique by Kraus et al. (2011). D_{sc} on Ganymede is $\sim 2 \text{ km}$ (Kraus et al. 2011) under its surface gravity, i.e., $\sim 1.425 \text{ m s}^{-2}$ (Anderson et al. 1996). Using this, we can compute D_{sc} for MU69 as $\sim 2 \text{ km} \times g_{\text{Gany}}/g_{\text{MU69}}$, where g_{Gany} and g_{MU69} are the surface gravities of Ganymede and MU69, respectively. If ρ_t for MU69 is 500 kg m^{-3} , given the equivalent radius of MU69, R_M , as $\sim 8.573 \text{ km}$, the surface gravity is $\sim 1.198 \times 10^{-3} \text{ m s}^{-2}$, and D_{sc} is $\sim 2378 \text{ km}$. In our simulations, Equation (7) yields $D_f/D_{tr} \sim 1.2$, which is consistent with Melosh (1989).

2.2. Dynamics and Structure Model (Model II)

Model II computes the minimum cohesive strength required for the neck to avoid structural failure during the Maryland impact, c^* . To determine the structural failure condition of the neck, we use the Mohr–Coulomb yield criterion, which is given as

$$\tau = \sigma \tan \phi + c, \quad (8)$$

where τ is shear stress, σ is normal stress, ϕ is the angle of friction fixed at 35° (Lambe & Whitman 1969), and c is cohesive strength. To determine σ and τ during the Maryland impact, we consider a force balance condition (Figure 1). Because the cavity of Maryland faces almost perpendicular to the long axis of MU69 (Stern et al. 2019), the impactor is assumed to impact on the smaller lobe in the normal direction to that axis. We assume a zero-obliquity impact case for simplicity while nonzero cases may be possible (e.g., Melosh 1989).

The impact-driven force, f_{imp} , is the time derivative of the change in the linear momentum of a target. The magnitude of this linear momentum change is equal to that of the linear momentum of the impactor, $p = m_i v_i$, where m_i and v_i are the mass and speed of the impactor, respectively. v_i is assumed to be 2.0 km s^{-1} , which is consistent with a typical impact speed in KBOs (e.g., Johnson et al. 2016). Note that the momentum transfer effect is not assessed in the present model, although it may generate an additional linear momentum (e.g., Holsapple & Housen 2012; Cheng et al. 2018; Hirabayashi et al. 2019a). Because the linear momentum may be delivered over the entire body as a form of wave propagation, f_{imp} may depend on how waves reach the neck region from the impact site. In a solid medium like the structure of MU69, an impact-generated stress wave, which consists of elastic and plastic waves, is always faster than a sound wave; as it grows in strength, the plastic wave catches up and surpasses the elastic wave by forming a shock wave (Melosh 1989). We compute a lower limit of f_{imp} by averaging p over the time when a sound wave goes from one side to the other in the smaller lobe, Δt :

$$f_{\text{imp}} \sim \frac{p}{\Delta t}, \quad (9)$$

where $\Delta t \sim 2R_S/C_{0r}$.

The normal force along the long axis of MU69, f_{norm} , is affected by the gravity force and the centrifugal force:

$$f_{\text{norm}} \sim \left| G \int_L \int_S \frac{d_{SL}}{d_{SL}^3} dm_S dm_L \right| - \frac{m_S m_L}{m_S + m_L} (A + R_S) \omega^2, \quad (10)$$

where m is the mass of each lobe, and the subscripts S and L indicate parameters for the smaller lobe and the larger lobe respectively. d_{SL} is a vector from an element in the smaller lobe to that in the larger lobe, and d_{SL} is its scalar value. G is the gravitational constant, A is the semimajor axis of the larger lobe, and ω is the spin rate of MU69 (the spin period, P_r , is 15.92 hr; Stern et al. 2019). We use an elliptical integral algorithm (Press et al. 2007) to compute the gravity term. We note that f_{norm} becomes positive during compression.

Using these force elements, we can calculate $\sigma = f_{\text{norm}}/S$ and $\tau = f_{\text{imp}}/S$, where S is the area of the contact between the larger lobe and the smaller lobe. Based on the reported shape model (Stern et al. 2019), we determine $S \sim 0.25\pi \times (36.3\% \times 20 \text{ km}) \times (50\% \times 7 \text{ km}) = 80 \text{ km}^2$. Finally, we obtain c^* as

$$c^* = \frac{f_{\text{imp}}}{S} - \frac{f_{\text{norm}}}{S} \tan \phi. \quad (11)$$

Given the present settings, the derived value of c^* may be a lower limit of the actual cohesive strength.

2.3. Integration of Models I and II

We now integrate Models I and II. In this integration, we assume $Y \sim c^*$ by considering Y to represent the strength of surface materials at zero pressure, which is equivalent to the cohesive strength. In Equation (7), the final crater is a function of r_i , ρ_t , and c^* . Because the Maryland crater is 7 km in diameter, we can use this equation as a constraint on these

properties:

$$D_f = h_I(r_i, \rho_t, c^*) = 7 \text{ km}. \quad (12)$$

On the other hand, Equation (11) is a function of r_i and ρ_t , which is given as

$$c^* = h_{II}(r_i, \rho_t). \quad (13)$$

Given the bulk density, we can implicitly solve these equations to compute r_i and c^* . All the defined parameters for solving these equations are given in Table 1.

We investigate how c^* and r_i vary as a function of ρ_t , given the defined endmember groups (Figure 2). c^* increases with ρ_t due to gravitational and centrifugal forces (Equation (11)) even though a higher-bulk-density target may create a smaller crater (Equation (6)). The size of a crater is smaller on a porous sand target (Wünnemann et al. 2006) than on a water-ice target (Kraus et al. 2011). Because the structure of MU69 is icy and highly porous (Stern et al. 2019), the actual values of c^* and r_i for MU69 may be placed between the endmember groups. We obtain that c^* is always higher than the order of kPa in the considered bulk density range.

The results show that the cohesive strength of MU69 may be higher than that of the reported small bodies. Small rubble pile asteroids are typically observed to have cohesive strengths of $\sim 300 \text{ Pa}$ or lower (e.g., Hirabayashi et al. 2014, 2019b; Scheeres et al. 2019; Watanabe et al. 2019), and so does the cometary nucleus of 67P (Hirabayashi et al. 2016). There are exceptional objects having a cohesive strength up to 1 kPa (Polishook et al. 2016). A ballistics analysis of the Deep Impact ejecta also showed that the cohesive strength of the nucleus of comet 9P/Tempel 1 may likely be less than $\sim 340 \text{ Pa}$ (Richardson et al. 2007). We note that Richardson et al. (2007) introduced an effective strength, which was defined as $K_2 Y$. $K_2 > 30$ in our analysis, and they estimated an upper limit of the effect strength as 10 kPa, leading to a cohesive strength of this nucleus less than $\sim 340 \text{ Pa}$. Also, the cohesive strength of ice rubbles is around 1 kPa, depending on the shear speed (Ettema & Urroz 1989). Finally, while the impactor's speed and bulk density are fixed at 2 km s^{-1} and 2000 kg m^{-3} , respectively, their variations do not change c^* by an order of magnitude. As these parameters change, the impactor's size should also be adjusted to generate a 7 km diameter crater on the smaller lobe. This mechanism does not change p much.

3. Discussion and Conclusion

Our model argued a discrepancy between the cohesive strength of MU69 and that of small bodies observed at high resolution. One explanation is that MU69's neck is strong enough to resist structural disturbance by the Maryland impact. This explanation, however, is inconsistent with the present knowledge about the cohesive strength in small bodies.

3.1. Breakup Scenario Driven by the Maryland Impact

We propose a scenario that, due to the Maryland impact, the neck fails structurally and loses its strength to hold the positions of the larger lobe and the smaller lobe. These two lobes can freely move to settle into a stable shape configuration where the energy is lowest (Scheeres 2007). We compute the bulk density that makes the current bilobate shape stable by using the energy analysis approach by Scheeres (2007). This approach can give proper shape equilibria of bilobate shapes at

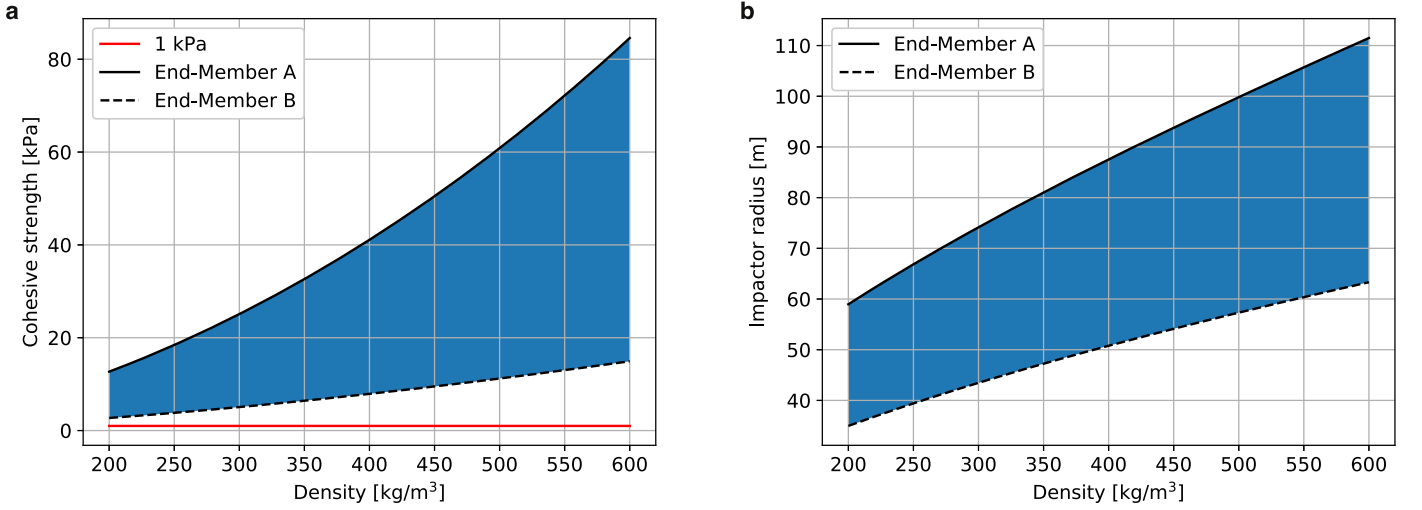


Figure 2. Impact cratering condition as a function of the bulk density. (a) Distribution of c^* . The red line shows a limit of the reported cohesive strength of small bodies. (b) Distribution of r_i . The shaded region is between the endmember groups.

Table 1
Parameters Used in the Present Model

Parameter	Model	Description	Value	Units	Reference
ϕ	I	Angle of friction	35	[deg]	Lambe & Whitman (1969)
ρ_i	I, II	Bulk density of impactor	2000	[kg m ⁻³]	[-]
v_i	I, II	Impact speed	2.0	[km s ⁻¹]	Johnson et al. (2016)
κ	I	Empirical parameter	1.19	[-]	Kraus et al. (2011)
η	I	Empirical parameter	0.04	[-]	Kraus et al. (2011)
C_Y	I	Empirical parameter for porous water ice	0.01	[-]	Arakawa & Yasui (2011)
β_Y	I	Empirical parameter for porous water ice	1.2	[-]	Arakawa & Yasui (2011)
C_{Or}	I, II	Speed of sound in MU69	1.85	[km s ⁻¹]	Arakawa & Yasui (2011)
C_{Oi}	I	Speed of sound in impactor	4.50	[km s ⁻¹]	Arakawa & Yasui (2011)
R_M	I	Equivalent radius of MU69	8.57	[km]	Stern et al. (2019)
A	II	Semimajor axis of the larger lobe	11	[km]	Stern et al. (2019)
R_S	II	Equivalent radius of the smaller lobe	6.3	[km]	Stern et al. (2019)
S	II	Neck area	80	[km ²]	Stern et al. (2019)
P_r	II	Spin period of MU69	15.92	[hr]	Stern et al. (2019)
Porous Sand Material in the Gravity Regime					
C_g	I	Empirical parameter	0.478	[-]	Wünnemann et al. (2006)
β_g	I	Empirical parameter	0.495	[-]	Wünnemann et al. (2006)
μ	I	Empirical parameter	3.95×10^{-1}	[-]	Wünnemann et al. (2006)
γ	I	Power index	2.42	[-]	Arakawa & Yasui (2011)
K_1	I*	Empirical parameter	6.01×10^{-1}	[-]	Wünnemann et al. (2006)
K_2	I*	Empirical parameter	3.04×10^1	[-]	Arakawa & Yasui (2011)
Water-ice Material in the Gravity Regime					
C_g	I	Empirical parameter	2.05	[-]	Kraus et al. (2011)
β_g	I	Empirical parameter	0.480	[-]	Kraus et al. (2011)
μ	I	Empirical parameter	3.81×10^{-1}	[-]	Kraus et al. (2011)
γ	I	Power index	2.50	[-]	Arakawa & Yasui (2011)
K_1	I*	Empirical parameter	2.55	[-]	Kraus et al. (2011)
K_2	I*	Empirical parameter	1.01×10^2	[-]	Arakawa & Yasui (2011)

Note. If necessary, the π -scaling parameters are derived under the assumption that the target bulk density is 500 kg m^{-3} . These parameters are indicated by adding asterisks in the model column.

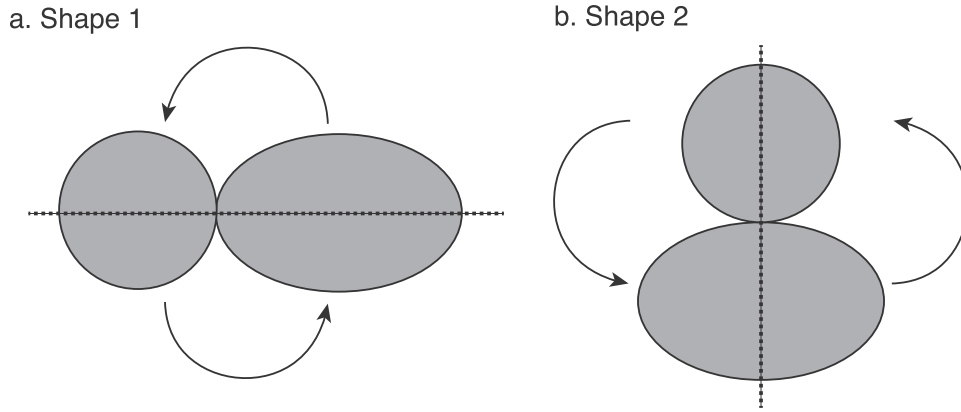


Figure 3. Possible shape configurations. The arrows show the directions of rotation. These shapes exist at different energy levels at a constant angular momentum.

different spins when two components are considered to be a sphere and a triaxial ellipsoid. This shape assumption simplifies the calculation of the system’s energy.

We compare the energy levels of two shape equilibria that MU69 possibly had before the Maryland impact event (Figure 3). Shape 1 corresponds to the current configuration in which the smaller lobe is resting on the long axis of the larger lobe (Stern et al. 2019). Shape 2 is a condition in which the smaller lobe is on the intermediate axis of the larger lobe. If MU69 had had Shape 2 initially, the spin period at that time would have been ~ 14.70 hr, given the current angular momentum. Note that we omit another configuration that the smaller lobe is on the short axis (Scheeres 2007) because only either Shape 1 or Shape 2 can energetically be lowest in the current problem.

We plot the shape equilibria as functions of the bulk density and the spin period (Figure 4). To develop this plot, we compute the energy with a constant angular momentum at each bulk density. Then, we calculate the spin periods of Shapes 1 and 2. The orange area means that regardless of MU69’s initial shape, Shape 1 is energetically lower, so the shape eventually settles into Shape 1. The blue region indicates that Shape 1 becomes lower only if MU69’s original shape is Shape 1. In other words, if MU69’s original shape is Shape 2, the shape is still stable and so does not change to Shape 1. This difference comes from our consideration of the two shapes at a given bulk density and a given angular momentum. Also, because the body experiences fission at fast rotation, the spin period should not be shorter than the fission limit.

3.2. Implication of the Merging Process

Because this shape sorting process should be satisfied anytime, the observed spin state may be indicative of the condition during the formation of the original bilobate shape of MU69, which is consistent with the interpretation by Stern et al. (2019). The Maryland impact cannot significantly change MU69’s rotational state. Even when we consider the highest linear momentum input case in our study, i.e., an impactor with a radius of 111 m, the spin period change of MU69 with Shape 1 is only ~ 4 minutes. This fact infers that MU69 has never experienced Shape 2 in its history. Therefore, it is likely that MU69 originally had Shape 1, the neck broke up, and each component was slightly reconfigured to settle into the current shape. This leads to a bulk density between 300 and 500 kg m^{-3} , which is reasonably consistent with that of the nucleus of 67P, i.e., $\sim 530 \text{ kg m}^{-3}$ (Sierks et al. 2015; Thomas et al. 2015).

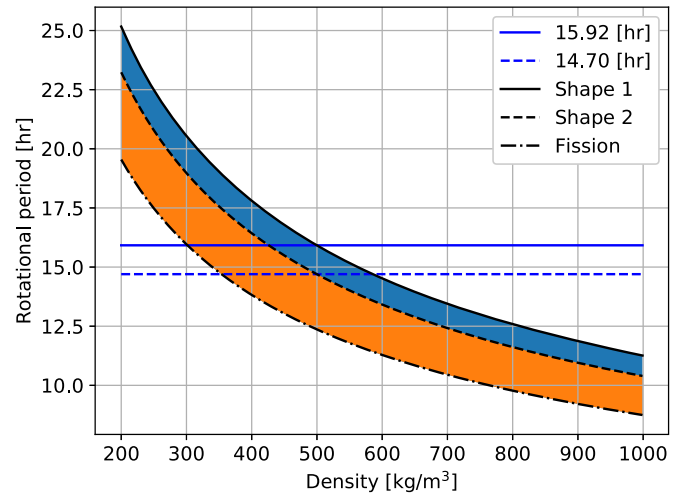


Figure 4. Minimum energy shape equilibria as functions of the bulk density (the x axis) and the rotational period (the y axis). The black solid and dashed lines describe the spin periods of Shapes 1 and 2, respectively, when the energy levels become the same for these shape configurations. The dotted-dashed line indicates the fission limit. Also, the blue horizontal lines give the spin period of each shape configuration given the current angular momentum.

3.3. Possibility of High Cohesive Strength in MU69

Importantly, we do not rule out that MU69, a representative of the classical KBO population and related populations at comparable sizes (Centaur, Trojans), possesses higher cohesive strength. Different levels of cohesive strength may induce various formation and evolution processes of primordial bodies. With higher cohesive strength, close binary systems in which two elements eventually collide with each other can form contact binaries more easily because their contact points can resist structural failure. Also, as such bodies consist of mixtures of volatiles and dust, it is likely that such various components may play a different role in cohesive strength in bodies from in other comets and asteroids.

3.4. Summary and Unresolved Issues

Considering that Maryland formed after the formation of MU69’s bilobate shape, we present that the impactor likely gave MU69’s neck strong structural disturbance, and the necessary cohesive strength to resist this event may be much higher than the reported strengths of small bodies observed at high resolution. While the scenario of MU69’s high cohesive strength cannot be ruled out, it may also be possible for MU69

to break up and resettle into the current shape. In this case, we can give constraints on the bulk density of MU69 ($300 \leq \rho_t \leq 500 \text{ kg m}^{-3}$). This discussion can be applicable to its soft-merging process of primordial elements.

We address two issues on the current study. First, it is uncertain whether the scaling relationships used are applicable to materials in MU69, which consist of a mixture of volatiles and dust (Stern et al. 2019). In fact, those for water ice were derived at a much higher temperature than MU69's surface temperature, $\sim 30 \text{ K}$ (Arakawa & Yasui 2011; Kraus et al. 2011). Second, our model simplified the force input by averaging over the timescale of wave propagation, although its time variation is likely to be critical. We leave these issues as a future study.

M.H. acknowledges support from NASA/Solar System Workings (NNH17ZDA001N/80NSSC19K0548). A.J.T. is supported by NASA/Earth and Space Science Fellowship (80NSSC18K1265). M.H. and D.B. are also supported by Auburn University/Intramural Grant Program.

ORCID iDs

Masatoshi Hirabayashi  <https://orcid.org/0000-0002-1821-5689>

Alexander J. Trowbridge  <https://orcid.org/0000-0002-7832-1387>

Dennis Bodewits  <https://orcid.org/0000-0002-2668-7248>

References

- Anderson, J. D., Lau, E. L., Sjogren, W. L., Schubert, G., & Moore, W. B. 1996, *Natur*, **384**, 541
- Arakawa, M., & Yasui, M. 2011, *Icar*, **216**, 1
- Birnstiel, T., Fang, M., & Johansen, A. 2016, *SSRv*, **205**, 41
- Bodewits, D., Farnham, T. L., Kelley, M. S. P., & Knight, M. M. 2018, *Natur*, **553**, 186
- Cheng, A. F., Rivkin, A. S., Michel, P., et al. 2018, *P&SS*, **157**, 104
- Christensen, N. I. 1966, *JGR*, **71**, 5921
- Davidsson, B. J. R., Sierks, H., Guttler, C., et al. 2016, *A&A*, **592**, A63
- Ettema, R., & Urroz, G. E. 1989, *Cold Regions Science and Technology*, **16**, 237
- Fraser, W. C., Bannister, M. T., Pike, R. E., et al. 2017, *NatAs*, **1**, 0138
- Hirabayashi, M., Davis, A. B., Fahnstock, E. G., et al. 2019a, *AdSpR*, **68**, 2515
- Hirabayashi, M., & Scheeres, D. J. 2019, *Icar*, **317**, 354
- Hirabayashi, M., Scheeres, D. J., Chesley, S. R., et al. 2016, *Natur*, **534**, 352
- Hirabayashi, M., Scheeres, D. J., Gabriel, T., et al. 2014, *ApJL*, **789**, L12
- Hirabayashi, M., Tatsumi, E., Miyamoto, H., et al. 2019b, *ApJL*, **874**, L10
- Holsapple, K. A. 1993, *AREPS*, **21**, 333
- Holsapple, K. A., & Housen, K. R. 2012, *Icar*, **221**, 875
- Jacobson, S. A., & Scheeres, D. J. 2011, *Icar*, **214**, 161
- Johansen, A., Oishi, J. S., Mac Low, M.-M., et al. 2007, *Natur*, **448**, 1022
- Johnson, B. C., Bowling, T. J., Trowbridge, A. J., & Freed, A. M. 2016, *GeoRL*, **42**, 10068
- Jutzi, M., & Benz, W. 2017, *A&A*, **597**, A62
- Kraus, R. G., Senft, L. E., & Stewart, S. T. 2011, *Icar*, **214**, 724
- Lambe, T. W., & Whitman, R. V. 1969, *Soil Mechanics* (New York: Wiley)
- Melosh, H. J. 1989, *Impact Cratering: A Geologic Process* (Oxford: Oxford Univ. Press)
- Morbidelli, A., & Nesvorný, D. 2019, arXiv:1904.02980
- Nesvorný, D., Youdin, A. N., & Richardson, D. C. 2010, *AJ*, **140**, 785
- Polishook, D., Moskovitz, N., Binzel, R. P., et al. 2016, *Icar*, **267**, 243
- Press, W. H., Teukolsky, S. A., Vetterling, W. T., & Flannery, B. P. 2007, *Numerical Recipes: The Art of Scientific Computing* (3rd ed.; Cambridge: Cambridge Univ. Press)
- Richardson, J. E., Melosh, H. J., Lisse, C. M., & Carcich, B. 2007, *Icar*, **190**, 357
- Scheeres, D. J. 2007, *Icar*, **189**, 370
- Scheeres, J., McMahon, J. W., French, A. S., et al. 2019, *NatAs*, **3**, 352
- Schenk, P., Beyer, R., Beddingfield, C., et al. 2019, *LPI*, **2132**, 2934
- Schwartz, S. R., Michel, P., Jutzi, M., et al. 2018, *NatAs*, **2**, 379
- Sierks, H., Barbieri, C., Lamy, P. L., et al. 2015, *Sci*, **347**, aaa1044
- Singer, K. N., McKinnon, W. B., Spencer, J. R., Weaver, H. A., et al. 2019, *LPI*, **2132**, 2239
- Stern, S. A., Weaver, H. A., Spencer, J. R., Olkin, C. B., et al. 2019, *Sci*, **364**, eaaw9771
- Thirouin, A., & Sheppard, S. S. 2019a, *AJ*, **157**, 228
- Thirouin, A., & Sheppard, S. S. 2019b, *AJ*, **158**, 53
- Thomas, N., Sierks, H., Barbieri, C., et al. 2015, *Sci*, **347**, aaa0440
- Vogt, C., Laihem, K., & Wiebush, C. 2008, *ASAJ*, **124**, 3613
- Watanabe, S., Hirabayashi, M., Hirata, N., et al. 2019, *Sci*, **364**, 268
- Wünnemann, K., Collins, G. S., & Melosh, H. J. 2006, *Icar*, **180**, 514